



# Manufacture of tunnel-shaped sheet metal parts with improved accuracy using novel toolpath strategies for single point incremental forming

Amar Kumar Behera<sup>1</sup> · Filip Lagodziuk<sup>2</sup>

Received: 27 September 2023 / Accepted: 21 June 2024 / Published online: 1 July 2024  
© The Author(s), under exclusive licence to Springer-Verlag London Ltd., part of Springer Nature 2024

## Abstract

Single point incremental forming is a novel sheet metal forming process that crafts 3D shapes out of sheet metal using layerwise deformation of the metallic sheet with a simple tool, which is typically cylindrical with a hemispherical ball-end. In this work, a combination of intelligent clamping and toolpath strategies was used to manufacture tunnel-shaped parts using aluminium alloy, AA1050AH14. The toolpath strategies helped improve on the low forming limits for failure typically associated with the manufacture of such shapes. A new method for compensating the inaccuracies in the parts caused by springback and other plastic deformations associated with the process using predicted 2D sectional views was also tested. The predicted sectional views were generated using training sets from the scanned geometries consisting of large datasets of point clouds. The training sets helped generate multivariate regression equations which were then used to create the predicted sections. The predicted sections were interpolated to create compensated geometries which then enabled part manufacture with improvement in accuracy. The result from this new strategy was compared with improvements observed in 3D compensation followed by adaptive pocketing and contouring toolpath strategies.

**Keywords** Single point incremental forming (SPIF) · Tunnel parts · Toolpaths · Compensation · Multivariate adaptive regression splines (MARS) · Pocketing · Contouring

## 1 Introduction

In recent years, single point incremental forming (SPIF) has come forth as a flexible, dieless sheet metal forming process that utilises the principles of computer numeric controlled (CNC)

machines to craft 3D shapes out of sheet metal using layerwise deformation of the metallic sheet using a simple tool, which is typically cylindrical with a hemispherical ball-end [1]. This process has been examined closely over the last two decades, leading to improved understanding of the deformation mechanics and process limitations in terms of sheet thickness variations, forming limits and achievable accuracy [2]. Multiple variants of the basic forming process have been explored such as the use of electrical heating [3] and laser support [4] to improve formability, ultrasonic vibrations [5], double-sided forming [6] and hybridisation with processes such as stretch forming [7].

Typically, SPIF has been used to form 3D sheet metal parts that have closed, continuous cross-sections perpendicular to the forming axis. As such, research on SPIF has primarily focused on forming fully constrained sheets, which are clamped on all four sides, creating parts that have the shape of a container post-forming. The disadvantage in forming container shapes is the waste of material when manufacturing products whose eventual shape is not meant to be a container and being limited with the product dimensions. Hence, recent research has started looking at the forming of tunnel-shaped parts [8]. Applications

### Highlights

- Manufacture of tunnel-shaped parts using single point incremental forming.
- Parts made using aluminum alloy, AA1050AH14.
- Toolpath strategies tested to prevent low forming limits and enhance accuracy.
- New sectional 2D-slice based compensation strategy developed to improve accuracy.
- Benchmarking accuracy against reprocessing and regression-based compensation.

✉ Amar Kumar Behera  
amarkb@iitk.ac.in

<sup>1</sup> Department of Design, Indian Institute of Technology, Kanpur, Uttar Pradesh 208016, India

<sup>2</sup> Department of Mechanical Engineering, Woodhouse Lane, University of Leeds, Leeds LS2 9JT, UK

of such tunnel shapes include crawl tunnels for children, cable trays, transmission tunnels for race cars and street machines, rollforming lines for metal shuttering, bio-medical implants and thin sheet moulds [9], as shown in Fig. 1.

Early design rules and process modelling techniques for tunnel and semi-tunnel parts were discussed by Afonso et al. [14]. However, this work did not illustrate any improvement in process outcomes such as geometric accuracy or improved formability. Leem et al. demonstrated the manufacture of corrugated structures using a Regional Plastic Incremental Bending (RPIB) strategy that uses a forming tool and a supporting tool to create tunnel-like shapes which had improvements in maximum deviations that were higher than a mm for aluminium alloy, AA5754-O and AA7075-O sheets [15]. While there is a marked improvement in the accuracy using such a technique, its limitation lies in the ability to create a two-tool-based setup to achieve such an improvement. In the absence of such a setup, in order to use the SPIF process specifically for making tunnel shapes without tooling changes that convert it into a double-sided process, there is a need for investigating other techniques such as 3D shape compensation functions [16, 17], multi-stage forming [18], soft computing approaches using neural nets [19] and support vector machines [20] to be able to realise geometric accuracy improvement.

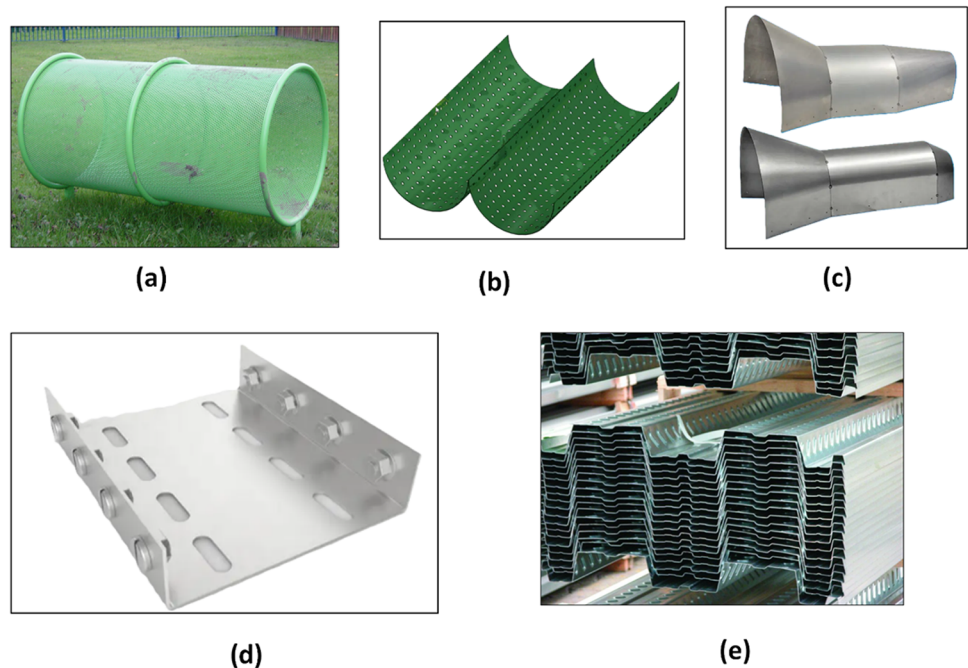
Early work on geometric accuracy in SPIF had looked into the use of counter dies, online profile measurement and correction, optimised toolpaths, optimisation of forming parameters, etc. [21, 22]. The limitations of these techniques were overcome by some of the later work that took into account the complexity of a network of features in the part using graph topology [23], use of mesh morphing techniques

[24], statistical optimisation [21], etc. Hussain et al. looked into the effect of five parameters, viz. sheet thickness, tool radius, step size, wall angle and pre-straining level of sheet on geometric accuracy and found that the sheet thickness, wall angle, step size and the interaction between the sheet thickness and wall angle had significant effect on the final geometric accuracy [21]. Sbayti et al. [25] carried out a Box-Behnken design of experiments together with a genetic algorithm-based optimisation to find out the optimised tool diameter, friction coefficient and increment step size that affected three process outcomes simultaneously, viz. forming force, final achieved depth and final sheet thickness [25]. However, due to the lack of a proper computer-aided process planning tool, this study was limited to only improving the depth accuracy rather than the accuracy of the whole part.

Gupta et al. manufactured channel shapes for aerospace applications and found that strain localisation at the corners of such shapes resulted in part failure [26]. They reported that both formability and geometric accuracy needed to be accounted for simultaneously in making such shapes. Excessive thinning at the edges leading to part failure in tunnel-shaped parts was reported by Afonso [27]. This work also reports that forming limits of tunnels are much more reduced than container type parts and the geometric accuracy is also worse. The forming of aluminium alloy AA 1050-H111 parts of 2-mm thickness and a tunnel width of 100 mm results in a maximum forming angle of  $68^\circ$ , which is  $8^\circ$  lower than that reported for container-type parts by Verbert [28]. As such, there is a key research gap in addressing the twin issues of formability and low accuracy simultaneously.

The tunnel shapes (see examples from this research in Fig. 2) were achieved by using semi-constrained sheets with only two

**Fig. 1** Various applications of tunnel-shaped sheet metal parts: **a** crawl tunnels for children [10], **b** CAD models for the crawl tunnels showing manufacture as two halves which can be formed separately, **c** transmission tunnels for automobiles [11], **d** cable tray [12] and **e** rollforming lines for metal shuttering [13]



sides of the blank sheet clamped and the other two free. This usually results in a lower formability and parts fail at a lower critical wall angle at failure. Additionally, the deformation mechanics are different from container-type parts leading to accuracy of the final formed shape being of a different magnitude and shape as compared to forming a fully constrained sheet.

To address the research gap surrounding issues related to the deformation mechanics in tunnel-shaped sheet metal parts, this work explored the effect of various toolpaths on the accuracy and formability of these parts. The aim of the current study was to investigate the effect of semi-constraining on the achievable part accuracy and improve part accuracy using novel toolpath strategies. Tunnels with planar side walls and varying wall angles made of aluminium alloy AA1050AH14 were formed and their accuracy behaviour was studied. The formed surfaces were compared to their nominal 3D computer-aided design (CAD) models. The accuracy data from these experiments were used to train a regression model using multivariate adaptive regression splines (MARS). This model was then used to predict the part accuracy of formed parts outside the training sets. These predictions were used to compensate the original CAD model using a known 3D compensation strategy [29] and a new 2D slice-based strategy to create compensated CAD models. The compensated models were used for optimised toolpath generation using two different toolpath strategies, viz. (i) contouring and (ii) adaptive pocketing. The accuracy results of the compensated parts formed using the various techniques were then compared to yield insights for optimised tunnel manufacture.

## 2 Methodology

An experimental setup with a dedicated rig for incremental forming was developed. Toolpaths were generated using different strategies such as contouring and adaptive pocketing with stepdowns in the  $z$ -axis varied at various locations. Part

compensation was done using a software tool that works on part geometries in stereolithographic (STL) file format. The data from the experiments was used to predict the accuracy using MARS. This was then used together with conventional 3D compensation and a novel 2D slice-based compensation, which is covered next.

### 2.1 Experimental setup

First, a dedicated rig was designed for manufacturing the parts. Experimental tests were performed on a XYZ 2500 SMX CNC milling machine. Parts were made from aluminium alloy, 1050AH14 sheet of 2-mm thickness which were cut to dimensions of  $155^{+0.1}_{-0.1}$  mm  $\times$   $155^{+0.1}_{-0.1}$  mm. The tolerances on the sheet thickness were observed to be  $\pm 0.05$  mm. A 10-mm spherical tip punch was used with a feed rate of 2000 mm/min with a spindle speed of 200 rpm and using ROCOL V-cut MP oil as a lubricant. To make tunnel shapes, the sheet was clamped only on two sides and two backing plates were used, one for each top edge of the tunnel (Fig. 3). Truncated tunnel-shaped pyramids with planar side walls and wall angles  $25^\circ$ ,  $30^\circ$  and  $40^\circ$  were formed to be used as training sets and analysed for their accuracy behaviour. A pyramid with wall angle  $35^\circ$  was used to validate the model created by using the training sets and test for accuracy improvement or deterioration.

### 2.2 Toolpath generation for tunnel-shaped parts

Three types of toolpath strategies were experimented with. These are shown in Fig. 4. In the first strategy, a contouring toolpath with stepdown of 1 mm in the  $z$ -axis located at the edges of the planar faces was used. This toolpath strategy uses alternating directions in each forming step, with the travel from one wall of the tunnel to the opposite made outside the part edge, as shown in Fig. 4a. In the second strategy, a contouring technique was used with stepdown of 1 mm located

**Fig. 2** Tunnel shapes formed as part of this work **a** placed horizontally after forming and **b** placed vertically under a GOM laser scanner

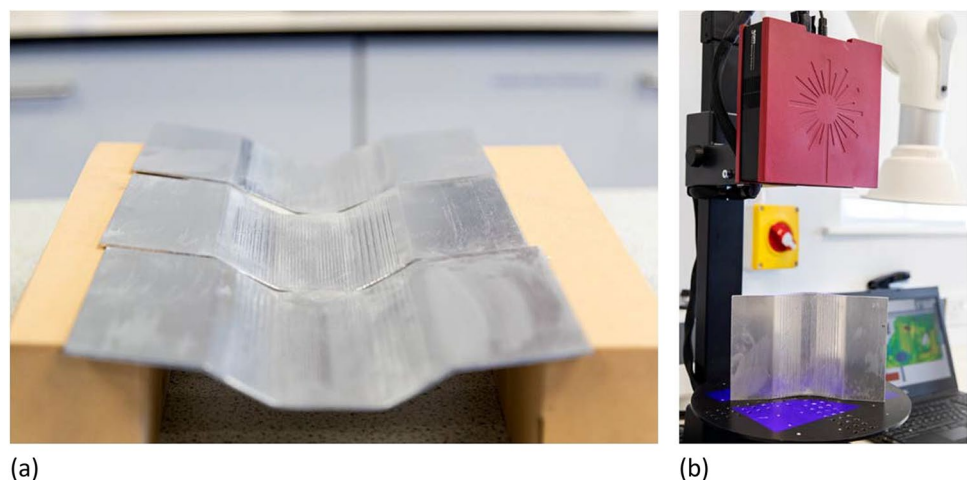
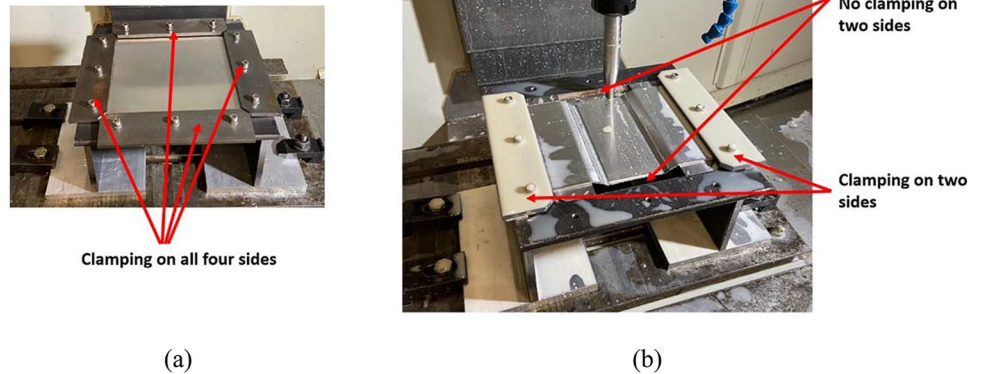


**Fig. 3** Incremental sheet forming rig showing **a** setup for container type parts and **b** setup for non-container tunnel-shaped parts



at the mid-section of the planar face. This meant that for each pass, half of the length was repeated, as shown in Fig. 4b. In the third strategy, an adaptive pocketing toolpath was used, where the tool went around the entire geometry in closed loops with a stepdown location and depth selected by the CAM software, Autodesk Inventor, as shown in Fig. 4c.

The toolpath programming for contouring toolpaths used customised programming using FSPIF, a Visual C# software tool that takes as input the geometry of the part defined in stereolithographic (STL) files, where the 3D shape is broken down into triangles with vertices and normals [29]. For the contouring toolpaths in Fig. 4a, the CAD model surface was extended by 5 mm on each edge (to allow a side changing position outside the true part edge) and a constant Z strategy was applied. The direction of tool travel for the even steps was then changed with stepdown at the edges (Fig. 4a). The toolpaths were post-processed to a numeric G-code to be run on the CNC milling machine.

### 2.3 Feature detection on STL files

The accuracy of parts made using SPIF depends on the geometrical features being formed [23]. Behera et al. identified

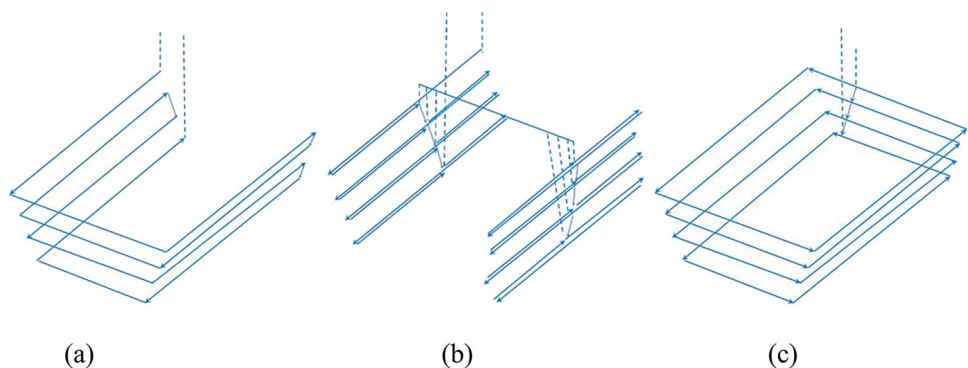
a taxonomy of 33 features where the classification was based on geometry, curvature, orientation, location and process-related attributes [30]. These features can be identified in FSPIF.

The feature recognition process is carried out by calculating the principal curvatures at each individual vertex of the STL file. This is done by following the steps outlined by Lefebvre et al. [31]. The curvature tensor at a vertex ‘ $v$ ’ of the STL model is calculated as follows:

$$\Lambda(v) = \frac{1}{|A|} \sum_{\text{edges}} \beta(e) \|e \cap A\| \frac{ee^T}{\|e\|^2} \quad (1)$$

where  $|A|$  is the surface area of the spherical zone of influence of the tensor and  $\beta(e)$  is the signed angle between the normal vectors of the STL facets connected by the edge  $e$ .  $\beta(e)$  is positive for a concave surface and negative for a convex surface. The factor,  $e \cap A$ , gives the weight for the contribution by an individual edge. The normal at each vertex is estimated as the eigenvector of  $\Lambda(v)$  calculated by the eigenvalue of minimum magnitude. The remaining eigenvalues,  $k^{\min}$  and  $k^{\max}$ , represent the minimum and maximum curvatures at the vertex  $v$ . Using these principal curvatures, four types of features can be classified as defined below:

**Fig. 4** Toolpath strategy for tunnel-shaped parts illustrating **a** contouring toolpath with stepdown at the edges of the tunnel, **b** contouring toolpath with stepdown at the mid-section of the tunnel planes and **c** pocketing toolpath that goes around the entire geometry including the non-formed areas



- *Planar feature*:  $k^{\min} = 0 \pm \epsilon_p$  and  $k^{\max} = 0 \pm \epsilon_p$ , where  $\epsilon_p$  is a small number that can be tuned for identifying planar features.
- *Ruled feature*:  $k^{\min} = 0 \pm \epsilon_r$  and  $k^{\max} = X$ , where  $X$  is a positive non-zero variable. Another possible case is where  $k^{\min} = X$  and  $k^{\max} = 0 \pm \epsilon_r$ , where  $X$  is a negative non-zero variable.  $\epsilon_r$  is a small number that can be tuned for identifying ruled features.
- *Freeform feature*:  $k^{\min} = Y \pm \epsilon_f$  and  $k^{\max} = X \pm \epsilon_f$ , where  $X$  and  $Y$  are non-zero variables such that  $X \leq \rho_{\max}$  and  $Y \leq \rho_{\min}$ , where  $\rho_{\max}$  and  $\rho_{\min}$  are threshold values for distinguishing freeform and rib features.  $\epsilon_f$  is a small number that can be tuned for identifying freeform features.
- *Rib feature*:  $k^{\min} \leq \rho_{\min}$  and/or  $k^{\max} \geq \rho_{\max}$

### 2.4 Accuracy predictions using multivariate adaptive regression splines

The accuracy of sheet metal parts formed by SPIF can be predicted using regression models generated from accuracy data obtained by scanning a set of formed parts that serve as training sets. Typically, this accuracy data is obtained by using a dimensional metrology touch probe or a laser scanner that creates a point cloud of the formed part. This point cloud is usually made of many points (100,000–500,000) and can be meshed to create a stereolithographic (STL) file where the points are joined together to form triangles that represent the surface of the formed part. This mesh can be compared to the original CAD model of the part to yield deviations at each individual point in the part. The deviations are then exported as a text file. The deviations are then linked to normalised parameter estimates on the nominal model to create another text file where each deviation corresponds to values of specific predictor variables, such as the distance to the edge of the feature and the distance to the bottom of the feature, as shown in Fig. 5. Next, the text

files from the training sets are post-processed in a statistical software to create the regression models.

As the features formed in the current study are all planar, the initial set of parameters that were used is as follows:

1. Normalised distance from a vertex to the edge of the feature in the tool movement direction:

$$d_b = \frac{D}{C + D} \tag{2}$$

2. Normalised distance from a vertex to the feature bottom:

$$d_o = \frac{B}{A + B} \tag{3}$$

3. Total vertical length of the feature at the vertex:

$$d_v = A + B \tag{4}$$

4. Total horizontal length of the feature at the vertex:

$$d_h = C + D \tag{5}$$

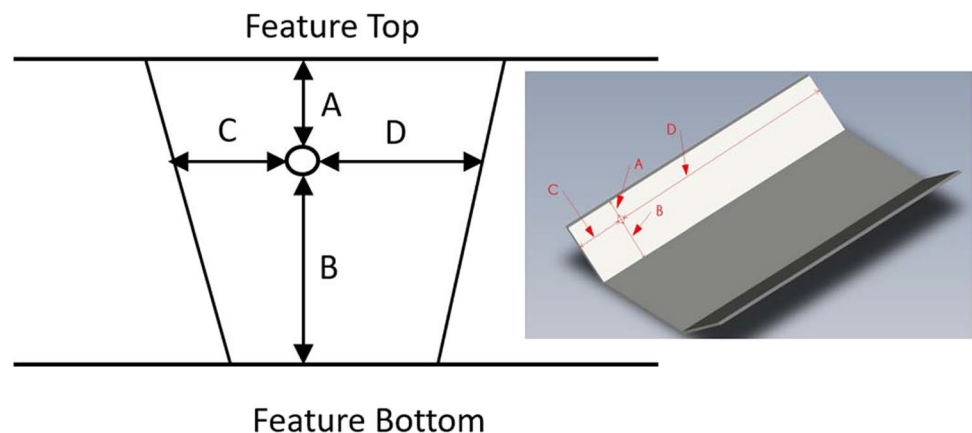
5. Wall angle at the vertex (in radians):  $\alpha$

One technique for creating the regression models for parts made by SPIF is multivariate adaptive regression splines (MARS) [29]. MARS is a non-parametric regression technique that analyses a data set to discover the best possible relationship between the predictor variables and a response variable. It generates a response surface with continuous first-order derivative. MARS models take the form:

$$\hat{f}(x) = \sum_{n=1}^N c_n B_n(x) \tag{6}$$

where the response variable is a weighted sum of basis functions  $B_n(x)$ , and the coefficients  $c_n$  are constants. The basis function  $B_n(x)$  takes on one of three forms:

Fig. 5 Distance parameters for creating regression models



- i. a constant,
- ii. a hinge function of the type  $\max(0, x - c)$  or  $\max(0, c - x)$ , where  $c$  is a constant and  $\max(p, q)$  gives the maximum of the two real numbers  $p$  and  $q$  or
- iii. a product of two or more hinge functions that models interactions between two or more variables.

The hinge functions consist of knots that are constants calculated using a forward pass step that initially over-fits the given data and then followed by a backwards pruning step which determines terms that are retained in the final model. The MARS models generated in this study were fitted using the ‘Earth’ library of R, which is a statistical software [32].

## 2.5 Compensation techniques

The accuracy prediction MARS models can be used to compensate for part accuracy by transforming the 3D CAD model of the part to be formed. Past work has looked at transforming the entire 3D CAD model based on predictions for every single point in the geometry [16]. This often has the effect of creating a distorted surface with sharp, uneven edges as the mathematical compensation cannot ensure that the normals of the compensated surface conform to a smooth surface. To get rid of the distortions in the compensated geometry, often a further smoothing step is required. That has the effect of creating a surface that may not be truly representative of the compensation required by the MARS model predictions. Hence, a new approach using accuracy predictions for 2D slices of the CAD model was developed in this study. The conventional technique and the new technique are discussed further below.

### 2.5.1 Conventional 3D compensation

Using the predicted deviation obtained from the MARS model for an unclamped part, every vertex on the STL file of the part to be formed is translated in a direction normal to

the feature on which it is present. This is illustrated in Fig. 6. The translated vertices are meshed to form the compensated model on which toolpaths are generated in a CAM software package such as NX or Autodesk Inventor. Typically, a compensation factor is used which can be tuned for different features, materials and sheet thicknesses. Mathematically, if the point on the nominal CAD model is denoted by the vector  $\vec{n}$ , the predicted point by the vector  $\vec{p}$ , then the predicted deviation  $\vec{d}$  is given by:

$$\vec{d} = \vec{p} - \vec{n} \quad (7)$$

The translated point,  $\vec{t}$ , is calculated as follows:

$$\vec{t} = \vec{n} - k\vec{d} \quad (8)$$

where ‘ $k$ ’ is the tuneable compensation factor.

The conventional compensation approach often results in a wavy surface profile, as shown in Fig. 7. This is because the points in the STL file have been translated individually based on a mathematical model without consideration for the smoothness and regularity of the compensated mesh that is generated from the translated points. While a local or global smoothing tool can be used to eliminate such errors, this can often be a time-consuming process and also deteriorate the accuracy of the compensated part.

### 2.5.2 Sectional 2D slice-based response surface fitting

To deal with the issues emerging from compensating a STL part model with ~ 10,000 to 500,000 points which leads to wavy or non-uniform surface geometry, a new technique was devised in this research. In this new technique, one or more sections of the compensated MARS model are extracted and then these sections are interpolated to form the compensated part file. The result of such interpolation using varying number of extracted sections is shown in Fig. 8. Several methods to interpolate between the compensated sections and the tunnel edge were experimented with. The use of the ‘lofted surface’ feature functionality within Solidworks and the ‘polygonize point cloud’ feature within GOM Inspect

**Fig. 6** Conventional 3D compensation illustrating translation of individual points on the STL file normal to the feature [29]; the predictions are made on the unclamped part

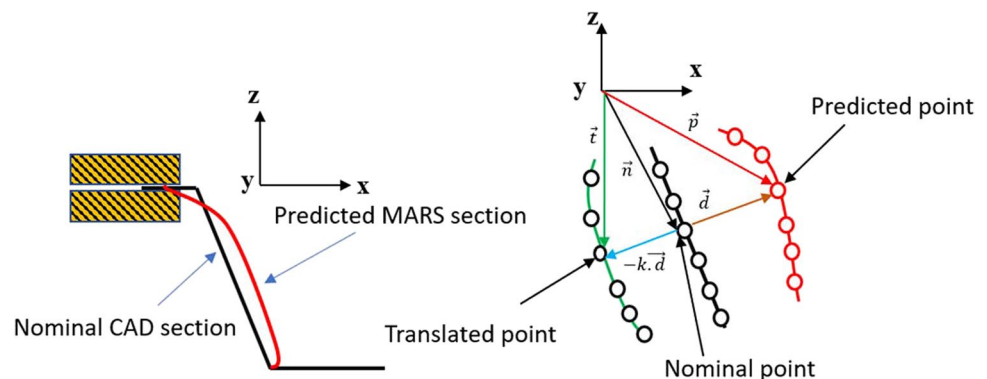


**Fig. 7** Issues with MARS compensation highlighting waviness and discontinuities in the toolpaths in **a** and **b** and in the compensated STL files in **c**; the red lines in **b** indicate the compensated profile while the blue lines indicate the nominal profile

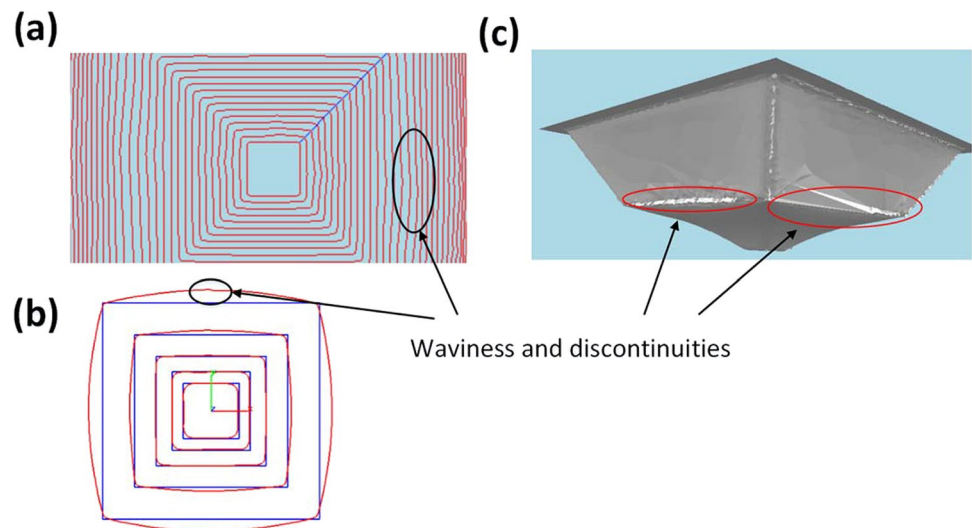
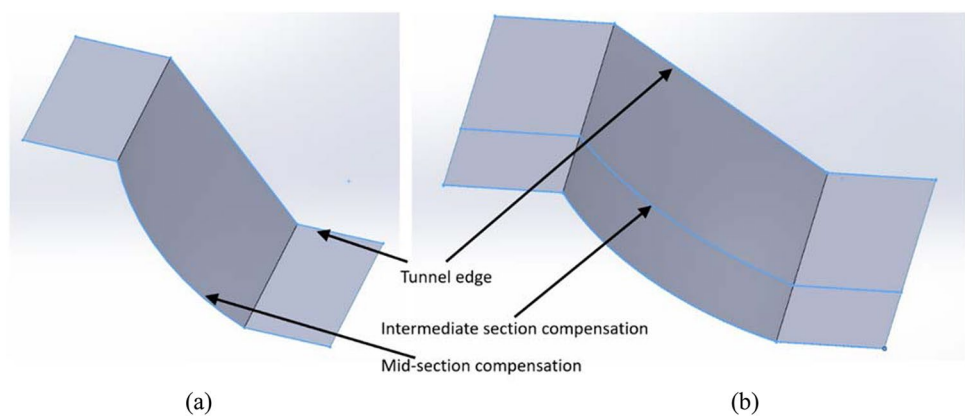


**Fig. 8** Compensation with 2D sectional slices and the tunnel edge showing use of **a** a single compensated mid-section and **b** two compensated sections



are examples of two techniques for creating the compensated final part.

### 3 Results

Accuracy results from uncompensated toolpaths were first analysed together with the effect of different types of toolpaths on part formability. These accuracy results were then linked to the detected features from the tunnels. These features with linked accuracy data resulted in the creation of the MARS models for error correction, which were then used to create compensated parts using both 3D compensation as well as the new technique that used 2D sectional slices.

#### 3.1 Accuracy analysis of uncompensated parts

The initial uncompensated part tests, using the contouring toolpaths shown in Fig. 4a, resulted in part failures at the edges of the tunnels (see Fig. 9). This was due to the step-down in the  $z$ -axis being programmed to be located at the

edges. This results in the stress magnitudes being high at these locations, where the sheet does not have any adjacent material on one side of the stepdown location. Hence, for subsequent tests, adaptive pocketing toolpaths with step-down locations away from the edges were generated, which helped avoid the failures at the edges (see Fig. 10).

Four uncompensated parts were made with wall angles varying between 25 and 40°. Adaptive pocketing toolpaths, shown in Fig. 4c, were used for these parts with varying step-down being determined by the Autodesk Inventor conforming to the part geometry. The formed parts were scanned with a GOM Atos Core 200 laser scanner and the resulting point clouds were meshed and compared with the nominal CAD models, resulting in accuracy plots as shown in Fig. 11. These accuracy plots were obtained after aligning the parts following a two-step alignment procedure in GOM Inspect, consisting of a pre-alignment step where the plane of the backing plate was used as the reference, followed by a best fit step. Once the nominal CAD model and measured point cloud mesh were aligned, the deviations were calculated by the GOM Inspect software by using the nominal

**Fig. 9** Uncompensated toolpath test results showing part failure at the edges where the stepdown in the  $z$ -axis is located

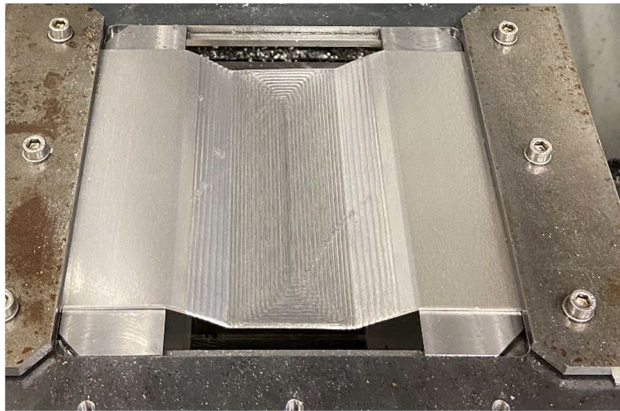
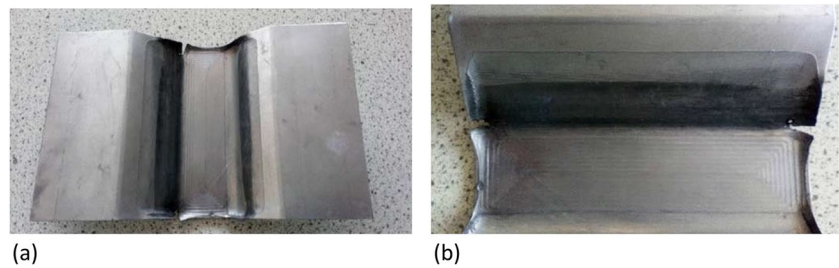


**Fig. 10** Uncompensated toolpath test results showing the use of an adaptive pocketing toolpath that prevents failure at the edges

model as the datum or reference. The accuracy data from these experiments, exported from within GOM Inspect as text files, was further analysed in MATLAB resulting in the deviations shown in Table 1. The key trend that was noted from these experiments was that both underforming and overforming increased with the wall angle being formed. The average positive and average negative deviations were higher with higher wall angles. Also, it was noted that the

deviations on the bottom of the part were significantly higher compared to toolpaths for fully constrained container type parts, which were formed using the setup shown in Fig. 3a. This was because the toolpaths used to avoid failure at the edges for tunnel-shaped parts needed pocketing approaches as compared to conventional contouring approaches that do not displace as much material towards the bottom.

### 3.2 Feature detection results

Features were detected on the STL files of the nominal models of the parts that were formed, using the software FSPiF. The detection of features followed the procedure outlined in Sect. 2.3 and using the taxonomy presented by Behera et al. [30]. The thresholds used for detection of tunnel-shaped truncated pyramidal parts were tuned for this geometry and are presented in Table 2.

The tuning process is required as the feature detection algorithm consists of an edge segmentation algorithm, followed by a region growing algorithm, as discussed in [30]. Vertices are added to a seed vertex based on their calculated Gaussian curvatures and neighbourhood. Depending on the thresholds that are set, a region may grow to cover a much larger area than it covers or be detected as a set of

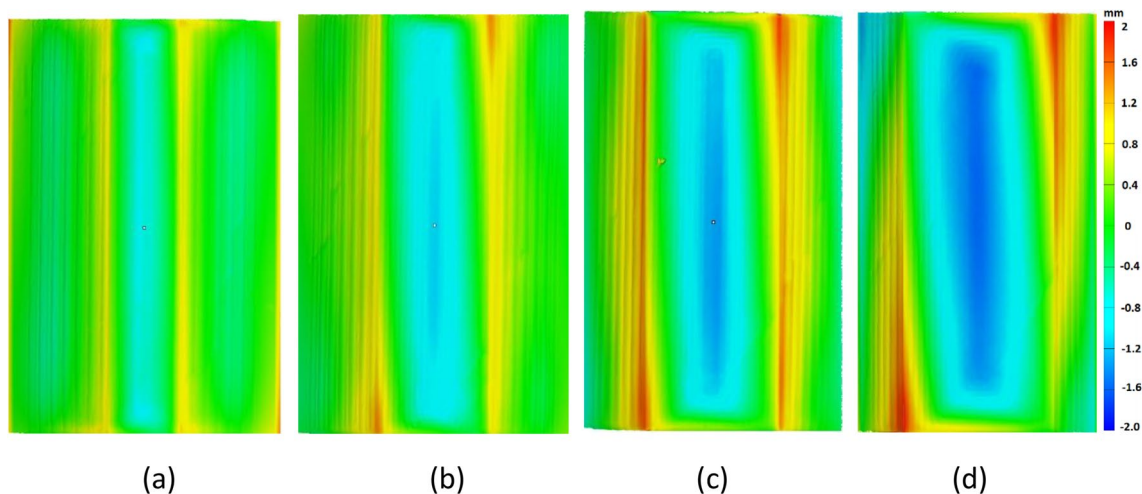


**Fig. 11** Accuracy plots for parts with wall angles **a** 25°, **b** 30°, **c** 35° and **d** 40°



**Table 1** Accuracies of manufactured parts without compensation

Wall angle (°)	Maximum deviation (mm)	Minimum deviation (mm)	Mean deviation (mm)	Average positive deviation (mm)	Average negative deviation (mm)
25	1.860	-0.852	0.011	0.379	-0.283
30	1.506	-1.142	0.021	0.389	-0.459
35	1.993	-1.367	0.055	0.648	-0.603
40	2.000	-1.575	0.043	0.784	-0.750

**Table 2** Feature detection thresholds

Threshold	Value
$\epsilon_p$	$5 \cdot 10^{-4}$
$\epsilon_r$	$10^{-5}$
$\epsilon_f$	$10^{-5}$
$\rho_{\min}$	-0.01
$\rho_{\max}$	0.01

neighbouring smaller features, both of which are not useful when it comes to applying feature-based compensation algorithms, based on the parameters which were defined in Sect. 2.4. With the tuned thresholds, an example of feature detection on a tunnel-shaped part is shown in Fig. 12.

One key observation for feature detection on shallow parts with low wall angles is that the bottom horizontal plane occasionally gets detected as an edge [33]. This is because only a small number of triangles are available for feature detection at the location where the ordinary non-horizontal planar (ONHP) feature meets the horizontal bottom planar (HBP) feature.

### 3.3 Error correction equation

The accuracy data from the three truncated pyramidal tests with wall angles 25°, 30° and 40° were used to train a MARS model in the statistical software ‘R’. The reason for using only 3 of the tests for training the model was to be able to use the 35° as a validation test case. Also, prior work has shown

that planar parts are well predicted using 3 training sets [16]. It may be noted that this multivariate regression predicts the error at a point and is based on point cloud data of nearly a million points from the 3 training set experiments and is regressed against 5 predictor variables. Due to the large number of points used to carry out this regression and statistical measures such as  $R^2$ , it has been proven to be a valid strategy.

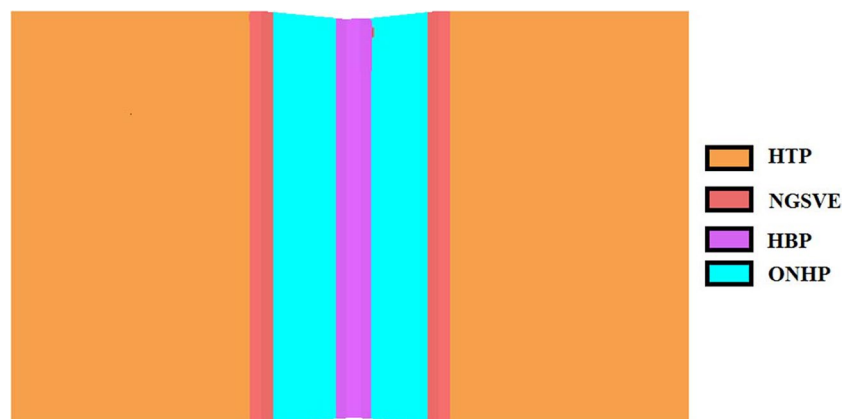
The following accuracy prediction equation, giving the error in mm, resulted from the MARS analysis ( $R^2=0.69$ ):

$$\begin{aligned}
 e = & 1.6 + 0.23 * \max(0, 0.53 - d_b) - 0.48 * \max(0, d_b - 0.53) \\
 & + 1.2 * \max(0, 0.59 - d_o) + 0.15 * \max(0, d_o - 0.59) \\
 & + 16 * \max(0, d_o - 0.93) - 44 * \max(0, d_o - 0.96) \\
 & - 0.15 * \max(0, 28 - d_v) - 0.31 * \max(0, d_v - 28) \\
 & - 6.6 * \max(0, 0.7 - \alpha)
 \end{aligned}
 \tag{9}$$

where  $d_b$  is the normalised distance from the point on the STL file to the edge of the feature in the tool movement direction,  $d_o$  is the normalised distance from the point to the bottom of the feature,  $d_v$  is the total vertical distance of the feature at the vertex in mm and  $\alpha$  is the wall angle at the vertex in radians.

It is worth noting here that the MARS method performs a forward pass and a backward pass. The forward pass adds basis functions in pairs and overfits the model. The backward pass prunes the model deleting the least effective term at each step until it finds the best sub-model. It is this process that eliminated one of the 5 predictor variables mentioned in Sect. 2.4. Furthermore, the different parameters may have different units

**Fig. 12** Feature detection results on a truncated pyramidal tunnel (the nomenclature used follows the shape feature taxonomy defined in [30]: *HTP*, horizontal top planar; *NGSVE*, negative general semi-vertical edge; *ONHP*, ordinary non-horizontal planar; *HBP*, horizontal bottom planar)



or be dimensionless but then there is a constant in front of each term, which can be thought of as having appropriate (e.g. units of mm or inverse units such mm/radian) such that each term in the predictor equation has dimensions of the predicted variable, which is the error in mm.

### 3.4 Results of conventional 3D compensation

The MARS model, shown in Eq. (9), was used to compensate the STL file of a part with wall angle  $35^\circ$  using the procedure outlined in Sect. 2.5.1. The result of this compensation for a section of the part geometry taken half-way through the tunnel for a compensation factor of +1 is illustrated in Fig. 13. The model was found to predict over forming in parts with low wall angles such as  $20^\circ$  and increasing under forming as the wall angle was increased in steps to  $40^\circ$ .

### 3.5 Results of sectional slice-based compensation technique

Using the technique described in Sect. 2.5.2, the same part with a wall angle  $35^\circ$  was compensated, as illustrated in Fig. 14. While the compensated coarse mesh had several areas with intersecting triangles and rough edges, the interpolated mesh using the slices did not have these artefacts, resulting in a smooth

surface profile on which the generated toolpaths did not show the waviness seen in the conventional 3D compensated parts. From a comparison of the prediction accuracies for varying number of slices (Table 3), it was seen that with increased number of slices, the accuracy of the interpolated mesh came closer to the MARS compensated mesh. However, for smoother meshes, a lower number of slices served best. Hence, there was a trade-off between obtaining a smooth surface vis-à-vis an accurate surface and the number of slices had to be selected carefully.

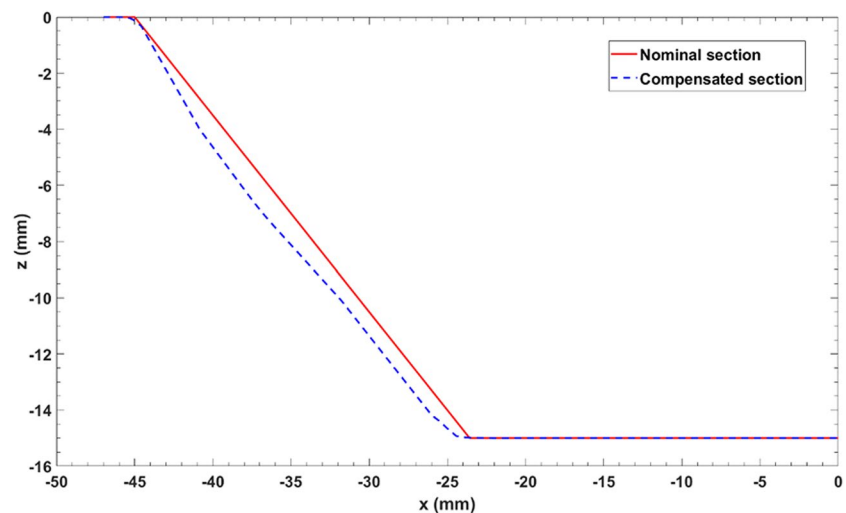
### 3.6 Testing and validation

The results of part compensation and reprocessing are presented in Table 4, while Fig. 15 shows the effect of the three accuracy improvement strategies including the new compensation technique on part accuracy. In addition to the pocketing toolpaths, contouring toolpaths with stepdown locations at the centre of the part were also tested. The effect of reprocessing on accuracy magnitudes was also studied.

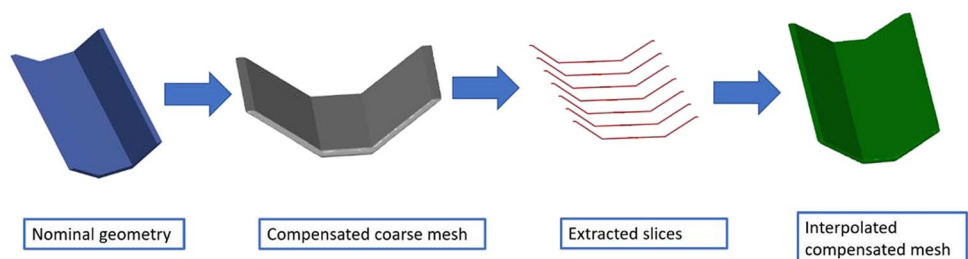
## 4 Discussion

The key challenge in this research was to simultaneously improve formability using novel toolpath selection and improve the accuracy at the same time. Contouring

**Fig. 13** Sectional view midway through the part at  $y=72.5$  mm from the part edge for a part with a length of 145 mm showing nominal and compensated sections



**Fig. 14** Part compensation using extracted slices from a compensated coarse mesh

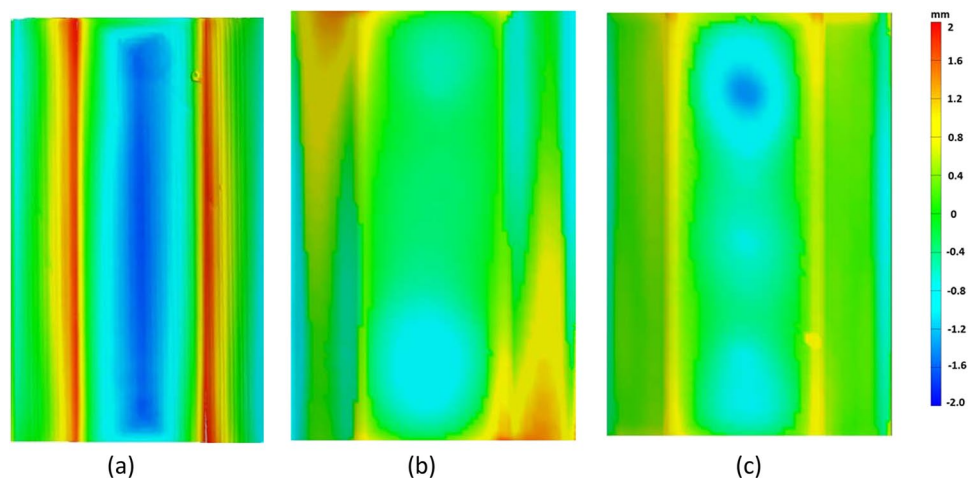


**Table 3** Prediction accuracies of meshes based on number of extracted slices (*all dimensions are in mm; the mesh generated from interpolating the extracted slices was compared to the MARS compensated mesh*)

Number of sections	Average deviation (mm)	Average positive deviation (mm)	Average negative deviation (mm)	Maximum deviation (mm)	Minimum deviation (mm)	Standard deviation (mm)
3	-0.0228	0.8091	-0.5365	1.9689	-1.4575	0.766
5	-0.0958	0.2388	-0.4366	1.1498	-1.4781	0.3416
7	0.1675	0.673	-0.4518	2.4917	-1.2693	0.6192
9	-0.0622	0.7152	-0.4726	1.9684	-1.2778	0.6587
11	-0.0117	0.1109	-0.1236	1.0476	-1.4143	0.152
13	-0.0161	0.0069	-0.081	0.4272	-1.078	0.0908
15	-0.01	0.0201	-0.0676	0.8972	-1.0035	0.0846

**Table 4** Results of reprocessing and compensation for a part with wall angle of 35°

Toolpath strategy	Compensation factor	Maximum deviation (mm)	Minimum deviation (mm)	Mean deviation (mm)	Average positive deviation (mm)	Average negative deviation (mm)
Uncompensated	0	1.993	-1.367	0.055	0.648	-0.603
Reprocessed	0	2.000	-1.677	-0.029	0.885	-0.768
3D MARS compensation—Pocketing	0.8	3.185	-0.930	0.264	0.565	-0.596
3D MARS compensation—Pocketing	1	1.165	-0.691	0.240	0.401	-0.417
3D MARS compensation—Pocketing	1.2	3.285	-0.663	0.333	0.514	-0.406
2D sectional compensation—Contouring	1	1.842	-0.896	0.071	0.467	-0.505
3D MARS compensation—Contouring	0.8	1.307	-0.559	0.076	0.309	-0.269

**Fig. 15** Accuracy colour plot showing the effects of **a** reprocessing and **b** sectional 2D slice-based compensation and **c** 3D MARS-based compensation

toolpath generation using conventional CAM packages with stepdown location at the edges of the tunnel shapes typically resulted in part failure beyond a specific depth. As such, tailored toolpaths were needed to prevent part failure. This was achieved using adaptive pocketing toolpaths, which were generated using Autodesk Inventor, and modified contouring toolpaths with stepdown locations at

the mid-section of the part generated using algorithms written in FSPIF, the Visual C# software for SPIF.

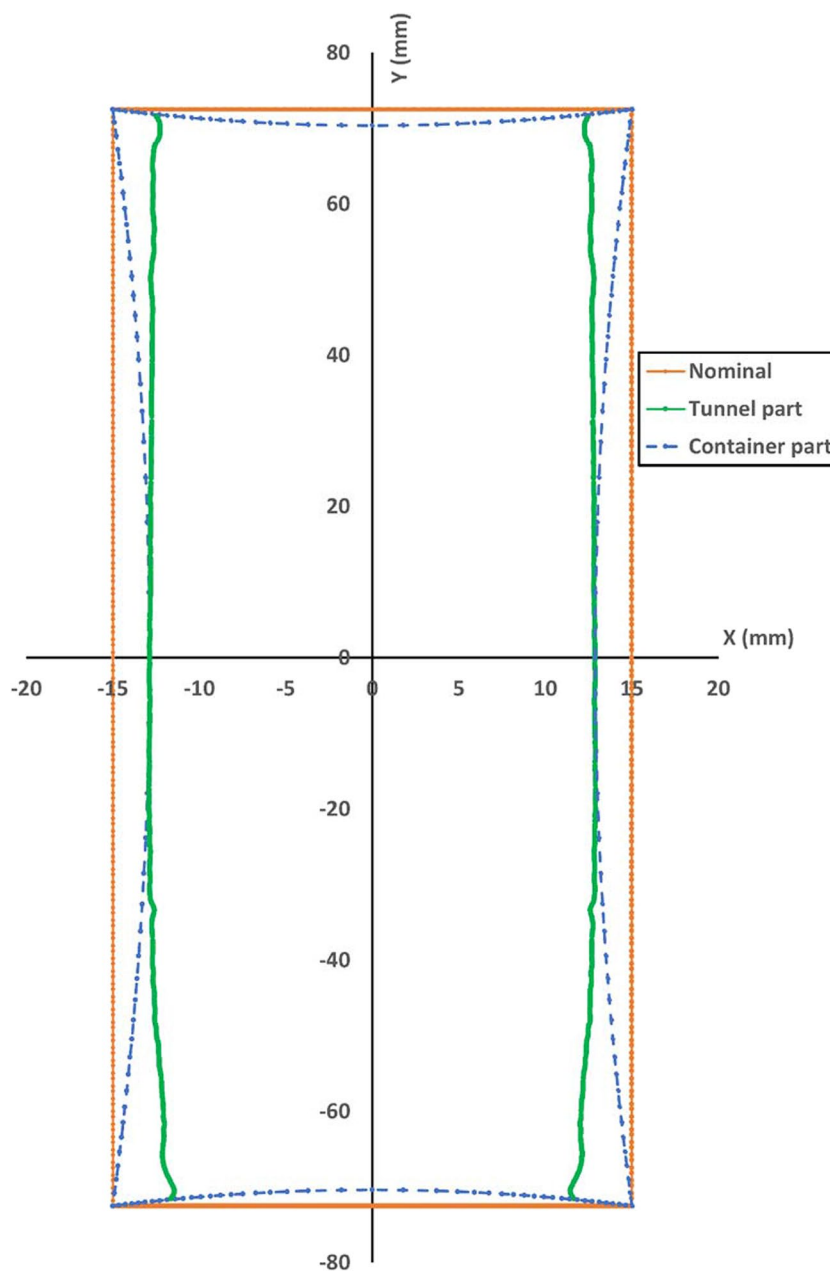
Furthermore, it was noted that accuracy behaviour of tunnel-shaped parts varies significantly from pyramidal parts, as seen from constant depth sections shown in Fig. 16. This is because the semi-vertical ribs that separate the planar faces in container type parts such as truncated pyramids module

the accuracy behaviours such that at the mid-section of the plane, the inaccuracy is the highest, while it drops to a minimum at the ribs, which are generally quite accurately formed due to their sharp curvature, as discussed previously in extensive detail by Behera et al. [29]. These ribs are not present in the tunnel-shaped parts and hence, the inaccuracy is the highest at the edges of the tunnels. Due to this distinct variation in accuracy in tunnel-shaped parts, which is the opposite of container-type parts, the compensation functions using MARS, as well as the compensation technique needs to account for these different accuracy behaviours.

While various approaches to improving accuracy in SPIF have been tried and tested, most of these techniques use

some form of tooling support, multiple toolpaths or a hybrid process that integrates SPIF with other process mechanisms [34]. Möllensiepe et al. looked into 19 different regression approaches that can help compensate toolpaths and ultimately concluded that regression methods need to be augmented with feature-based approaches [35]. This is because the stiffness of the sheet is different at various locations after clamping. Specifically, it is different at the top as compared to the bottom. In addition, features themselves tend to have different stiffnesses, such as semi-vertical ribs, which tend to be stiffer than planar and ruled features due to the difference in Gaussian curvatures [23]. Hence, feature-dependent parameters, such as the distance to the top, bottom and

**Fig. 16** Comparison of accuracy behaviours of container and non-container parts by taking sections at a specific depth ( $Z = 14$  mm) for a  $25^\circ$  wall angle part (the container part is a truncated pyramid with four walls while the non-container part is a tunnel-shaped part with two walls only)



ribs, used within a multi-variate regression model, such as MARS, tend to perform better than a featureless method.

The results for feature detection on truncated pyramidal parts as shown earlier by Behera et al. [23, 30] worked well for tunnel-shaped parts too. The detection thresholds did not vary much vis-à-vis fully constrained parts. The detection algorithms remained the same as well. It was noted that in some cases, the horizontal bottom planar feature was detected as an edge on account of low volume of triangulation for smaller parts. Besides, the transition from one plane to another induced a positive horizontal edge feature which kept growing in volume as the detection algorithm proceeded in these cases.

The results from the uncompensated tests indicate that both under forming and over forming increased with wall angle (Fig. 11). The average positive deviation increased from 0.379 to 0.784 mm while the average negative deviation increased from  $-0.283$  to  $-0.750$  mm (Table 1). The mean deviations increased systematically as well. There was significantly higher under forming observed in the bottom of the tunnel-shaped parts as compared to what would be expected for fully constrained parts. This was primarily in cases where pocketing toolpaths were used to avoid failure at the edges. The pocketing toolpaths displaced more material towards the bottom due to processing the entire sheet, as opposed to conventional contouring approaches that only process the planar faces.

The effect of reprocessing the part was to increase the over forming, while the under forming remained almost the same. Hence, for this set of parts, reprocessing was not able to improve the accuracy and rather deteriorated it. Using conventional 3D MARS compensation with pocketing toolpaths, a compensation factor of +1 worked best and improved the average positive deviation from 0.648 to 0.401 mm, while the average negative deviation also saw an improvement from  $-0.603$  to  $-0.417$  mm. For contouring toolpaths with compensation, a compensation factor of 0.8 saw an improvement of the average positive and negative deviations to +0.309 mm and  $-0.269$  mm.

The new technique using 2D sectional compensation also resulted in accuracy improvements to +0.467 mm and  $-0.505$  mm using a compensation factor of +1 and contouring toolpaths. It performed better than using 3D MARS compensation with pocketing toolpaths. This was because the pocketing toolpaths moved the material towards the bottom of the part by going around in loops around the entire sheet and depositing it there. This increased the pillow effect occurring at the bottom, thereby enhancing the overall under forming of the part. As such, the new sectional 2D slice-based compensation may be preferred to 3D MARS-based compensation with pocketing. While the 3D MARS-based compensation with contouring tool paths performed marginally better than the new technique, it has the disadvantage

of not being able to produce an even and smooth surface. Hence, for applications demanding a smooth surface finish, the new sectional technique may be preferred.

## 5 Conclusions

The manufacture of tunnel-shaped parts requires the tool-path generation to be specifically tailored to the geometry such that failure can be avoided at regions of high stresses, particularly at the edges. Adaptive pocketing toolpaths are particularly helpful in this regard, with the stepdown locations kept within the internal geometry of the part away from the edges. Likewise, contouring toolpaths with stepdown location in the mid-section of the planar features are also successful in distributing the stresses evenly and reducing the chances of part failure. However, toolpaths with step down locations at the edges are likely to result in failure after forming to a relatively small depth.

The accuracy behaviours of truncated tunnel-shaped planar features using single point incremental forming (SPIF) indicate some overlapping and some dissimilar trends as observed for fully constrained truncated pyramids. The similar trends include over forming at low wall angles and under forming at higher wall angles on the planar faces. However, the accuracy magnitudes at the bottom of the part are distinct from fully constrained parts due to different toolpaths needed to avoid failure at the edges of the tunnels. Feature detection on STL models of tunnel-shaped parts requires thresholds similar to fully constrained parts.

The use of conventional 3D compensation using multi-variate regression splines (MARS) to compensate for part accuracy in aluminium alloy, AA1050AH14 sheets, was tested and found to work best for a compensation factor of +1 for pocketing toolpaths and with a factor of +0.8 for contouring toolpaths. However, reprocessing of the tunnels did not result in improved accuracy. A new technique using sectional 2D slice-based compensation was tested and found to work well for a compensation factor of +1. It was also noted that three distance parameters and the wall angle of the part were the selected predictor variables in the MARS regression model.

Further work in this area can involve looking into the effect of material properties on compensation factors in improving part accuracy, building on limited past work on the effect of material properties [36]. Features may interact with one another [37] and as such, this can be studied by forming two slope tunnel-shaped planar features and interacting ruled and freeform surfaces that help understand the deformation mechanisms better, make good predictions and form complex parts. The effect of material properties and sheet thickness on accuracy profiles can be studied using digital image correlation leading to better predictions using generic error correction functions.

**Acknowledgements** The authors acknowledge the help provided by John Morris and Jakub Gacka of the University of Chester in setting up the experimental apparatus and conducting the experiments. The authors also acknowledge discussions with Daniel Afonso and Ricardo Alves de Sousa of the University of Aveiro, which helped shape this work.

**Author contribution** Dr Amar Kumar Behera contributed to the study conception and design and data analysis. Material preparation, data collection and analysis were performed by Filip Lagodziuk. The first draft of the manuscript was written by Dr Amar Kumar Behera and all authors commented on previous versions of the manuscript. All authors read and approved the final manuscript. The experimental work and early analysis were carried out at the University of Chester. Detailed final analyses and writing of the manuscript of this paper were done at IIT Kanpur.

**Funding** This work was supported by financial support from the University of Chester and by Indian Institute of Technology, Kanpur (grant numbers R&D-DESP-2023284 and IITK-DESP-2023107).

## Declarations

**Competing interests** The authors declare no competing interests.

## References

- Jeswiet J et al (2005) Asymmetric single point incremental forming of sheet metal. *CIRP Ann Manuf Technol* 54(2):623–649
- Gatea S, Ou H, McCartney G (2016) Review on the influence of process parameters in incremental sheet forming. *Int J Adv Manuf Technol* 87:479–499
- Fan GQ et al (2008) Electric hot incremental forming: a novel technique. *Int J Mach Tools Manuf* 48(15):1688–1692
- Duflou JR et al (2007) Laser assisted incremental forming: formability and accuracy improvement. *CIRP Ann Manuf Technol* 56(1):273–276
- Amiri S, HosseinpourGollo A, Paktinat H (2017) An investigation of conventional and ultrasonic-assisted incremental forming of annealed AA1050 sheet. *Int J Adv Manuf Technol* 90:1569–1578
- Peng W, Ou H, Becker A (2019) Double-sided incremental forming: a review. *J Manuf Sci Eng* 141(5):050802
- Araghi BT et al (2009) Investigation into a new hybrid forming process: incremental sheet forming combined with stretch forming. *CIRP Ann* 58(1):225–228
- Afonso D, de Sousa RA, Torcato R (2017) Incremental forming of tunnel type parts. *Procedia Eng* 183:137–142
- Appermont R et al (2012) Sheet-metal based molds for low-pressure processing of thermoplastics. in *Proceedings of the 5th Bi-Annual PMI Conference*
- Massey and Harris Engineering Ltd. (2024) Crawl tunnels. Available from: <https://www.masseyandharris.com/product/crawl-tunnel/> Accessed 28 March 2024
- Babco Media Inc. (2024) Chassisworks transmission tunnel kits. Available from: <https://www.enginebuildermag.com/2019/06/chassisworks-transmission-tunnel-kits/> Accessed 28 March 2024
- Baide CNC Ltd. (2024) High strength OEM Service frp fiberglass cable tray for tunnels sheet metal stamping. Available from: <https://www.baide-cnc.com/gallery/high-strength-oem-service-frp-fiberglass-cable-tray-for-tunnels-sheet-metal-stamping/> Accessed 28 March 2024
- STAM S.p.A. - Società per azioni a socio unico (2024) Rollforming lines for metal shuttering for concrete. Available from: <https://www.stam.it/en/roll-forming-lines-metal-shuttering-concrete/> Accessed 28 March 2024
- Afonso D, Alves de Sousa R, Torcato R (2018) Integration of design rules and process modelling within SPIF technology—a review on the industrial dissemination of single point incremental forming. *Int J Adv Manuf Technol* 94:4387–4399
- Leem D et al (2022) A toolpath strategy for double-sided incremental forming of corrugated structures. *J Mater Process Technol* 308:117727
- Verbert J et al (2011) Multivariate adaptive regression splines as a tool to improve the accuracy of parts produced by FSPIF. *Sheet Metal* 2011(473):841–846
- Carette Y, Vanhulst M, Duflou JR (2021) Geometry compensation methods for increasing the accuracy of the SPIF process. *Key Eng Mater* 883:217–224
- Bambach M, TalebAraghi B, Hirt G (2009) Strategies to improve the geometric accuracy in asymmetric single point incremental forming. *Prod Eng* 3(2):145–156
- Moses Raja Cecil D (2021) A MANFIS-based geometric deviation prediction and optimal parameter selection for SPIF geometric accuracy improvement. *Soft Comput* 25(23):14829–14840
- Romero PE et al (2021) Use of the support vector machine (SVM) algorithm to predict geometrical accuracy in the manufacture of molds via single point incremental forming (SPIF) using aluminumized steel sheets. *J Mater Res Technol* 15:1562–1571
- Hussain G, Lin G, Hayat N (2011) Improving profile accuracy in SPIF process through statistical optimization of forming parameters. *J Mech Sci Technol* 25(1):177–182
- Bambach M, Araghi BT, Hirt G (2009) Strategies to improve the geometric accuracy in asymmetric single point incremental forming. *Prod Eng Res Devel* 3(2):145–156
- Behera AK (2013) Shape feature taxonomy development for toolpath optimisation in incremental sheet forming. PhD Thesis. Katholieke Universiteit Leuven
- Behera AK, Lauwers B, Duflou JR (2014) Tool path generation for single point incremental forming using intelligent sequencing and multi-step mesh morphing techniques. *International Journal of Material Forming (Advanced Modeling and Innovative Processes)* 8:517–532
- Sbayti M et al (2018) Optimization techniques applied to single point incremental forming process for biomedical application. *Int J Adv Manuf Technol* 95(5):1789–1804
- Gupta P, Szekeres A, Jeswiet J (2019) Design and development of an aerospace component with single-point incremental forming. *Int J Adv Manuf Technol* 103:3683–3702
- Afonso D (2016) Incremental forming of tunnels. University of Aveiro
- Verbert J (2010) Computer aided process planning for rapid prototyping with incremental sheet forming techniques. PhD Thesis. Katholieke Universiteit Leuven.: Leuven
- Behera AK et al (2013) Tool path compensation strategies for single point incremental sheet forming using multivariate adaptive regression splines. *Comput Aided Des* 45(3):575–590
- Behera AK, Lauwers B, Duflou JR (2012) Advanced feature detection algorithms for incrementally formed sheet metal parts. *Trans Nonferrous Metals Soc China* 22:S315–S322
- Lefebvre PP, Lauwers B (2004) STL model segmentation for multi-axis machining operations planning. *Computer-Aided Des Appl* 1(1–4):277–284
- Milborrow S (2023) Package ‘earth’. 18–07–2023; Available from: <https://cran.r-project.org/web/packages/earth/earth.pdf>
- Behera AK et al (2018) Accuracy analysis of incrementally formed tunnel shaped parts. in *Recent Advances in Intelligent Manufacturing: First International Conference on Intelligent*

- Manufacturing and Internet of Things and 5th International Conference on Computing for Sustainable Energy and Environment, IMIOT and ICSEE 2018, Chongqing, China, September 21–23, 2018, Proceedings, Part I 5. Springer
34. Lu H, Liu H, Wang C (2019) Review on strategies for geometric accuracy improvement in incremental sheet forming. *Int J Adv Manuf Technol* 102(9):3381–3417
  35. Möllensiepe D et al (2020) Regression-based compensation of part inaccuracies in incremental sheet forming at elevated temperatures. *Int J Adv Manuf Technol* 109(7):1917–1928
  36. Behera AK et al (2012) Influence of material properties on accuracy response surfaces in single point incremental forming. *Material Forming - Esaform 2012, Pts 1 & 2, 504–506:919–924*
  37. Behera AK, Lauwers B, Duflou JR (2012) An integrated approach to accurate part manufacture in single point incremental forming using feature based graph topology. *Material Forming - Esaform 2012, Pts 1 & 2, 504–506:869–876*

**Publisher's Note** Springer Nature remains neutral with regard to jurisdictional claims in published maps and institutional affiliations.

Springer Nature or its licensor (e.g. a society or other partner) holds exclusive rights to this article under a publishing agreement with the author(s) or other rightsholder(s); author self-archiving of the accepted manuscript version of this article is solely governed by the terms of such publishing agreement and applicable law.